Microscaled design of the linear and non-linear optical properties of tantalum germanate glasses by thermal poling

Gael Poirier, Lara Karam, Vincent Rodriguez, Frédéric Adamietz, Thierry Cardinal, Fargin Evelyne, Marc Dussauze

Linear and non-linear optical microstructuring in sodium tantalum germanate glasses by thermal poling

Gael Poirier[1(*)], Lara Karam[2], Vincent Rodriguez[2], Frédéric Adamietz[2], Thierry Cardinal[3], Evelyne Fargin[3] and Marc Dussauze[2(*)].

[1] *Grupo de Química de Materiais, Universidade Federal de Alfenas, Campus de Poços de Caldas, Poços de Caldas-MG, Brazil*

[2] *Institut des Sciences Moléculaires, UMR 5255, Université de Bordeaux, 351 cours de la Libération, 33405 Talence Cedex, France.*

[3] *Institut de Chimie de la Matière Condensée de Bordeaux, Université de Bordeaux, 87 Avenue du Dr Schweitzer, F-33608, Pessac, France.*

E-mail: marc.dussauze@u-bordeaux.fr

Mail address: Institut des Sciences Moléculaires, UMR 5255, Université de Bordeaux, 351 cours de la Libération, 33405 Talence Cedex, France.

(*) Corresponding author.

E-mail: gael.poirier@unifal-mg.edu.br

Mail address: Instituto de Ciência e Tecnologia, Campus de Poços de Caldas – Poços de Caldas-MG, Brazil – CEP 37715-400.

(*) Corresponding author.

Abstract

Sodium tantalum germanate glasses were thermally poled using microstructured metallic anodes of two distinct geometries. Topological, structural and optical characterizations of the micro-imprinted structures revealed an accurate reproducibility of the electrode patterns on the glass surface with strong edge effects between the poled and unpoled areas. 100 nm-depth spatial reliefs were achieved and associated with glass network rearrangements due to sodium departure under the conductive anodic patterns. Second harmonic signals originating from both longitudinal and in-plane static electric fields were identified mainly near the borders of imprinted structures and related to a specific charge distribution model. Spatially controlled positive refractive index changes around 7 to 9.10^{-3} could be induced, opening opportunities for active optical devices operating in the middle infrared.

Keywords: Glass, germanate, thermal micropoling, second harmonic generation, refractive index.

1 – Introduction

Alkali niobium and tantalum germanate glasses are interesting materials thanks to their specific optical properties emerging from the mixed niobate/tantalate and germanate glassy network built upon MO_6 (M=Nb or Ta) and GeO_4 units [1-3]. In fact, several thermal and optical properties can be tuned by the M_2O_5 content along the glass forming domain. For example, low transition metal contents promote higher thermal stabilities against devitrification whereas higher contents close to the limit of the glass forming domain lead to strong crystallization tendency with formation of perovskite bronze-like crystalline phase of general formula $A_2M_8O_{21}$ where A is an alkaline ion, mainly Na or K [1,2,4,5]. Optical properties which make these materials promising for photonic applications include their transparency in the middle infrared up to 6 μm as well as the tunable rare earth visible and near infrared luminescent properties as a function of the M_2O_5 content or the degree of crystallinity in these compositions [2,3,6-9]. However, besides the design of suitable glass compositions with the required physical specifications, photonic technologies and integrated optics also bring the need for a more precise control and/or modulation of the linear and non-linear optical properties at the microscale. Among many physical and chemical methodologies developed for such purpose, thermal poling, which can be understood as the application of a strong DC electric field on a heated non-crystalline material (usually a glass), has attracted attention in the past few years [10-13]. First reports have demonstrated that such electric field applied on a glass heated below its glass transition temperature induce a migration of positive charges like alkaline ions from the anodic surface towards the cathode [14-17]. After cooling back the sample to room temperature and then removing the high voltage, this electric field assisted space charge induced under the anode surface is

"frozen" in the glass, generating a permanent static electric field (E_{int}). A few microns thick alkaline depleted layer with a high negative charge density is formed at the anodic side; it gives rise to specific modifications of the poled glass chemical and optical properties. For example, surface reactivity can be modified with respect to the atmospheric moisture resistance and/or hydrophobicity [18]. Thermal poling is also well known to promote second order non-linear optical properties such as second harmonic generation (SHG) associated with anisotropy generated orthogonally to the treated surface. Although some works suggest that SHG can be related with orientable species, it is well accepted that the main SHG mechanism is an electro-optic effect associated with the third order non-linear susceptibility $\chi^{(3)}$ and the internal electric field according to the relation $\chi^{(2)}=3.\chi^{(3)}.E_{int}$, called the EFISH model for Electric Field Induced Second Harmonic [14-17, 19]. Besides the non-linear optical properties associated with the space charge, cations depletion from the poled layer also promotes compositional changes associated with structural rearrangement for charge compensation [20, 21, 22-27]. Lower refractive indices are usually induced in the poled layer when compared to the pristine glass, opening opportunities for waveguides design [28,29]. Even though thermal poling is an outstanding tool for optical materials, photonic technologies are in need of a microscale control of the optical properties for microdevices suitable for integrated optics. In this sense, deep efforts have been made for miniaturization of the thermal poling principle on glass surfaces. Particularly, the use of micro structured electrodes with periodic conductive and insulating patterns has been proven useful for accurate micro-imprinting of the electrode structure on glass surfaces [30-33]. This approach, sometimes reported as thermal micropoling, allows the control of surface relief as well as linear and

non-linear optical properties at the microscale [33-37]. Charge distribution models are well described and accepted after classical poling treatment and are related with a homogeneous migration of mobile cations under the anode. However, thermal micropoling promotes more complex charge density distributions and strong edge effects between the poled and unpoled surfaces [36]. Microstructuring of chemical and optical properties has been achieved by thermal poling in silicate and phosphate glasses but has not been reported in germanate glasses yet, despite their broader optical window in the middle infrared and higher refractive index compared to other oxide glasses. Since recent investigations have shown that thermally poled sodium tantalum germanate glasses exhibit stable second harmonic generation associated with sodium depletion [38], the present work investigates in details the effect of microstructured anodes during thermal poling on topological and structural modifications, and on the localization and geometry of the second harmonic generation as well as the refractive index changes in sodium tantalum germanate glass compositions.

2 – Experimental Part

Glass samples of composition $75GeO_2$-$10Na_2O$-$15Ta_2O_5$ were prepared from reagent grades GeO_2 99,9%, Ta_2O_5 99,9% and Na_2CO_3 (from Sigma Aldrich Corp.). Starting powders were weighted and grounded in an agate mortar for a 30 g total batch and melted in a platinum crucible at 1500 ºC for 2 hours. In a second step, the crucible was cooled in cold water for 5 seconds and put in a furnace at 700 ºC during 12 hours for annealing before slow cooling to room temperature. The glass

sample formed in the crucible was then cut and polished for final glass sizes of 1 mm in thickness and 25 mm in diameter.

The microstructured anodes consisted of a 50 nm thick titanium layer (for mechanical adherence) and a 100 nm thick platinum film deposited on a glass slide that were lithographically structured. Two different periodic patterns were used in this work. The first electrode, labeled E-70/4, presented insulating squares of 70 μm (glass substrate free of metallic layer) separated by a 4 μm-large conductive grid as depicted in Figure 1a. The second electrode labeled E-4/4 was constituted of 4 μm diameter insulating circles distant of 4 μm one from the other (Figure 1c).The cathode was constituted of an n-doped silicon wafer under a 150μm-thick borosilicate coverslip employed to keep the optical quality of the glass on this side. The glass samples, respectively referred to as G-70/4 and G-4/4 depending of the anode employed for the treatment, are 1 mm-thick polished glass samples. They were pressed between two electrodes and heated from room temperature to 265 ºC at 5 ºC/min under flowing nitrogen atmosphere before applying a DC field between the electrodes during 30 min. The samples were then slowly cooled down with the DC field kept on until the sample reached room temperature. Based on previous studies [38], thermal poling treatments were first performed at 1350 V but the poled surface as observed by optical microscopy appeared strongly damaged. Decreasing poling voltages were tested until a clean microstructured surface was obtained for an 800 V poling voltage as illustrated by the Figure 1b and 1d for the samples G-70/4 and G-4/4 respectively.

Correlative Raman and SHG microscopies were recorded on the surface of the micropoled samples in backscattering mode using a modified micro-Raman spectrometer HR800 (Horiba/Jobin Yvon) equipped with a confocal microscope

and a (x,y,z) motorized stage enabling 3D mapping with a spatial resolution around 0.5 μm. Raman measurements were performed with a CW laser operating at 532 nm and a 1064 nm (ω) picosecond laser was used as the excitation source for μ-SHG mapping recorded at 532 nm (2ω). Two different incident polarizations were employed to probe the SHG signal namely azimuthal and radial polarizations. They were obtained using a polarization converter from Arcoptix relying on the special alignment of liquid crystal molecules. For both of them, the polarization states at the focal point were calculated following a methodology described in our previous work [12] and using a program developed by Li [39]. In the supplementary material S1, the intensity distribution profiles of the in-plane (I_{xy}) and out of the plane (I_z) components are shown for the two polarization states. They were calculated for a 100×-0.9NA air objective that was employed for the μ-SHG measurements of the G-70/4 sample and for a 100×-1.3NA oil objective that was used for the G-4/4 sample. These profiles show that the radial polarization allows for probing of the SHG response both in and out of the plane while the azimuthal polarization only probes the in-plane response.

Electrostatic simulations were achieved using the software COMSOL. Taking in account the electrode's geometry, we have calculated, for a wide range of charge distributions in the micropoled glasses, electrical potentials and electric field components. Calculation results were compared with SHG intensity profiles to give some insights about the poling patterning process. Atomic force microscopy (AFM) measurements were performed on the surface of the thermally poled glasses in PF-QNM (Peak Force Quantitative Nanoscale Mechanical characterization) mode using a Bruker Dimension ICON System and a PFQNE-AL cantilever. Refractive index changes along the imprinted microstructures were accessed by a phase contrast

technique: a wave-front sensor SID4Bio by Phasics Inc placed inside an optical microscope was used to record the phase image of the microstructures. This measurement was performed in transmission mode under white light illumination using a band pass filter centered at 750 nm through a 100×-1.3NA oil objective. The refractive index variations were calculated by dividing the optical path difference along the microstructures by the thickness of the poled layer (estimated around 2.5 μm by SHG microscopy on the micropoled glass cross-section).

3 – Results and discussion

Sodium tantalum germanate glass samples of composition $75GeO_2$-$10Na_2O$-$15Ta_2O_5$ were thermally poled at 265 ºC under a 800 V DC electric field using the E-70/4 and E-4/4 microstructured electrodes whose periodic patterns are presented in Figures 1a and 1c respectively. Optical micrographs of the surface of the corresponding poled glass samples are depicted in Figures 1b and 1d. The inset of Figure 1d also brings the visual aspect of the poled glass where the poled area is clearly identified due to visible light diffraction. Under these poling conditions the microscaled patterns of the electrodes were perfectly reproduced on the glass surface, pointing out that micro-imprinting by thermal poling is effective and reproducible in these sodium tantalum germanate compositions.

Micro-Raman mapping measurements were performed at the boundary between the zones in contact (poled zone) and not in contact (unpoled region) with the metallic portions of the electrode for a better understanding of the glass network structural modifications under thermal poling. An optical microscopy image of this region on the G-70/4 sample is presented in Figure 2a. Raman

mapping was performed in a 12 μm×35 μm area delimited by the yellow rectangle with a 1 μm step along the X and Y axis. Two Raman spectra collected from the unpoled region (far from the boundary) and the poled area (under the metallic part of the electrode) were extracted and are compared in Figure 2b. Despite the overall similarities of these spectral profiles which were normalized at the most intense signal (480 cm^{-1}), weak differences in several Raman mode intensities could be detected at 430 cm^{-1} (mode 1 in Figure 2b), 800 cm^{-1} (mode 2) and 1550 cm^{-1} (mode 3). Such weak variations on their own are hardly conclusive about structural changes promoted by thermal poling and could also be related with experimental conditions. However, Raman mappings comparing relative intensities of modes 1, 2 and 3 are depicted in Figure 2c1, 2c2 and 2c3 respectively and it appears that these signal intensities are well spatially correlated with the imprinted patterns. Previous μ-Raman investigations performed on homogeneously poled samples cross-section already related Raman mode variations centered at 430 cm^{-1} (mode 1) and 800 cm^{-1} (mode 2) to Ge-O-Ge bridging bonds in four-membered rings of GeO_4 tetrahedra [38, 40, 41] and Ta-O stretching modes in isolated TaO_6 units distributed inside the covalent germanate network [38,42,43], respectively. As reported, relative higher intensity of mode 1 after thermal poling can be interpreted by a polymerization of the germanate network where $Ge\text{-}O^-$ terminal bonds stabilized by Na^+ ions are converted to bridging Ge-O-Ge bonds in order to balance the sodium departure from the poled layer. On the other hand, a lower intensity in mode 2 suggests that tantalum oxide units are partially separated from the germanate network under thermal poling which promotes a nanoscaled phase separation between the germanate and tantalate species [38]. In the present work, similar spectral evolution are observed

even if the spectral variations are less pronounced than for a homogeneous poling probed on the cross section [38]. This can be explained by the difference in probing geometry between these two studies (cross section vs. along the surface). The weak spectral variations observed on a patterned glass surface are the consequence of the difference between longitudinal and in plane spatial resolution in confocal Raman microscopy as compared to the poled layer thickness. Besides these considerations, another weak Raman signal was detected around 1550 cm^{-1} only in the poled area as evidenced by Figures 2b and 2c3. This feature, already reported in poled silicate and phosphate vitreous layers is associated with symmetric stretching of trapped molecular oxygen and support the structural model of a partial conversion of $Ge\text{-}O^-$ terminal bonds in Ge-O-Ge bridging linkages where the remaining oxygens are oxidized to molecular oxygen for charge compensation mechanisms [23,24,36,44].

The static electric field resulting from poling is known to break the glass' centrosymmetry and induce otherwise forbidden second order optical response such as SHG. This response was probed using the confocal μ-SHG setup described in the experimental section with both radial and azimuthal incident polarizations. These results are gathered in the Figure 3 for both G-70/4 (Figures 3a) and G-4/4 (Figures 3b) glass samples. In each case, an optical micrograph highlights the areas (Figures 3a1 and 3b1) that were probed under radial and azimuthal polarizations with respective μ-SHG mappings, $I_{2\omega\text{-}rad}$ (Figures 3a2 and 3b2) and azimuthal, $I_{2\omega\text{-}azi}$ (Figures 3a3 and 3b3)

Let us first focus on the G-70/4 sample. The SHG response as probed under radial polarization is mainly localized at the poled/unpoled border (Figure 3a2), i.e. at the edges of the electrode's conductive part. In the poled zone (under the

conductive grid of the electrode), the SHG intensity decreases by a factor of four, while in the unpoled region, no SHG signal can be measured under this polarization. When probed under azimuthal polarization (Figure 3a3), the SHG response is also localized at the edges of the electrode's borders. No SHG signal can be measured in the poled zone nor in the unpoled region: under azimuthal polarization, the border between these two regions is the only SHG active zone. One must also note that, for the G-70/4 sample, there is a co-localization of the SHG response maxima as probed under the two polarizations. This behavior is different from the one observed for the G-4/4 sample. Indeed, on the G-4/4 sample, the SHG response as probed under radial polarization is maximal in the center of the circle. That is, surprisingly, in the region where the electrode is not conductive. On the other hand, the maximum SHG intensity probed under azimuthal polarization is localized all around the imprinted circle.

To recapitulate, the electrodes employed to pole these two samples present opposite patterns: E-70/4 is constituted of thin conductive parts and large non-conductive zones while E-4/4 is composed of roughly equivalently large conductive and non-conductive areas. The resulting micro-poled samples exhibit different electric field geometry as evidenced by the SHG mappings. For G-70/4, the maximal intensities as probed under radial and azimuthal polarizations are co-localized, while it is very clear that for G-4/4, they are not. In order to gain a precise understanding of the underlying charge distributions at the origin of these responses, an electrostatic model was developed on the basis of our previous work on borophosphate glasses[36]. The results of these calculations as well as a comparison with the experimental results are gathered in the Figure 4.

The Figures 4a and 4b correspond respectively to the glass samples G-70/4 and G-4/4. For both samples, a sketch of the charge density distributions employed to simulate the different observables is presented at the top of the figure (Figure 4a1 and 4b1). The micro structured poled layers were simulated using three different charge concentrations: a positive one, ρ_1 and two negative charge concentrations, ρ_2 and ρ_3. All possible combinations of charge concentrations range values were tested for the following set of values: [1.10^3; 3.10^3; 5.10^3; 7.10^3; 1.10^4] C/m^3 for ρ_1 , [-1.10^3; -3.10^3; -5.10^3; -7.10^3; -1.10^4] C/m^3 for ρ_2 and [-1.10^2; -1.10^3; -5.10^3; -1.10^4] C/m^3 for ρ_3 . For each cases the electrical potential, the electrical field in the plane (along X) and out of the plane (along Z) were calculated. In order to ascertain the charge distribution at the origin of the measured SHG signal, the square of the calculated electric field was compared to the measured SHG intensity.

As a recall, two different polarizations were employed to probe the SHG signal, namely radial and azimuthal polarizations. As illustrated by the point spread functions presented in the supplementary material, an azimuthal incident polarization allows for probing the response only in the plane while a radial polarization probes the response both in and out of the plane. Therefore, the SHG intensity measured under azimuthal polarization was confronted to the calculated E_x^2. The electric field along the Z axis is only be probed with a radial polarization, thus, the calculated E_z^2 was compared to the SHG intensity as measured under radial polarization.

In the Figure 4, are presented the results for a specific set of values for ρ_1, ρ_2 and ρ_3 that best reproduced the measured SHG signals: ρ_1=7E^3 C/m^3; ρ_2=-1E^4 C/m^3 and ρ_3=-1E^2 C/m^3 for the sample G-70/4 in Figure 4a5 and ρ_1=8E^3 C/m^3; ρ_2=-5E^3

C/m^3 and ρ_3=-5E^2 C/m^3 for the sample G-4/4 in Figure 4b5. For both electrode's geometries, the SHG signal is simulated with similar models, i.e. with similar charge distributions at the edges. The rather good correspondences observed for both samples denote that the spatial control of the SHG response can be understood and managed on the basis of the charge distribution along one single electrode's edge. For more complex electrode geometries, it can then be deduced constructing electrostatic models on the base of the charge distribution expected for one electrode's edge. This constitutes a promising finding for the accurate control of such an imprinting process.

It is worth noting that the charge distribution at the origin of the SHG response in these germanate glasses is slightly different from the one evidenced in borophosphate glasses [36]. Therefore, the way the glass reacts to this imprinting process depends on (i) the type of electrode and (ii) the glass composition. However, we would like to emphasize that for both glass families, the model is the same one, only varying slightly in charge volumic concentration and edges effects sizes. This points out again that such an approach using an electrostatic model to estimate the second order optical properties in thermoelectrically imprinted glassy materials is robust.

Topological effects of micro-imprinting by thermal poling were also investigated by Atomic Force Microscopy, these results are gathered in the Figure 5. Figures 5a, 5b and 5c present an optical image of the probed area, the corresponding AFM measured 3D image and a topology profile for sample G-70/4. The same investigation for the sample G-4/4 is presented in Figures 5d, 5e and 5f. For both samples, it appears that, in the poled area, the glass experiments a contraction with a depth variation of about 100 nm. AFM investigations also

evidence intense edge effects as can be seen in the Figures 5c and 5f. At the poled/unpoled frontier, stronger topology variations of the order of 300 nm are measured with a pronounced contraction on the conductive side of the conductive/nonconductive frontier and an opposite increase on the nonconductive side. This corresponds well to the charge distributions at the conductive/nonconductive borders presented in the Figure 4 and in particular the positive and negative charge accumulations at this frontier. Here, the topology of the poled glass seems to be modified by an electro-mechanical effect which is governed by charge accumulation and change of sign at electrode edges.

Since thermal micropoling promotes large compositional variations between poled and unpoled areas, linear optical properties should also be impacted by the treatment as already observed in other glassy systems [13]. In particular, the Figure 6 focuses on the refractive index modification and structuring induced by poling. In the Figures 6a and 6c are presented the top-view phase contrast images for samples G-70/4 and G-4/4 respectively. These images show the optical path difference (OPD) which is related to (i) the topology change and (ii) the poled layer thickness and its modified refractive index. They demonstrate that regular optical patterns are successfully produced by thermal micro-poling. Refractive index difference profiles could not be accurately obtained from the OPD since the strong topological variations at the poled/unpoled frontiers as well as the wavelength used for the phase contrast measurements do not give a reliable resolution around these areas. However, one could also disregard these edge effects and focus on the variation of the OPD between the center of the poled and the unpoled regions. With these considerations, as can be seen on the Figures 6b and 6d, the OPD is estimated to 60 nm for G-70/4 and to

45 nm for G-4/4. Considering a poled layer thickness of about 2.5 μm as measured for a homogenous poling [38], the refractive index difference Δn ($\Delta n=n_{poled}-n_{unpoled}$) between the unpoled and poled areas after topology correction (methodology described in Supplementary Material S2) can be estimated respectively to 9.5×10^{-3} and 7.1×10^{-3} for G-70/4 and G-4/4. Positive values of Δn point out a higher refractive index under the poled surface in these sodium tantalum germanate glasses, in opposition with refractive index decreases of the order of 10^{-2} observed in niobium borophosphate glasses [45]. Since usual Δn decreases after poling are attributed to a correlated local density drop due to sodium depletion, our results can be understood by a local compression of the glass structure under poling promoting a higher number of highly polarizable tantalum atoms per unit volume.

Anyway, positive Δn values of the order of 10^{-3} are compatible with waveguide production and reveal that the micro-imprinting process by thermal poling is a promising methodology for the microscale control of both linear and non linear optical properties.

4 – Conclusion

Glass samples of composition $75GeO_2$-$10Na_2O$-$15Ta_2O_5$ were prepared by the melt-quenching technique at 1500 °C and thermally poled using microstructured metallic electrodes. The electrode microscale patterns could be accurately reproduced over large areas at the surface of the glass. Structural rearrangements observed after poling were attributed to a sodium depletion out of the poled layer and consequent repolymerization of the germanate and tantalate glass network through conversion of terminal oxygens to bridging bonds and molecular oxygen. Local SHG signals related with both longitudinal and in-plane

static electric fields were evidenced out of the poled borders and were found to be confined over a 5 μm region. A model of charge density distribution explaining the second order non-linear properties is proposed for these specific glass composition and poling conditions. Topological effects were also characterized with a contraction of the poled surface of about 100 nm and strong edge effects of the order of 300 nm at the poled boundaries. Homogeneous optical contrasts could be produced along the imprinted patterns with a refractive index increase of about 8.10^{-3} in the poled layers. Our results support the efficiency of this glass composition and thermal micropoling for the design of microscale linear and non-linear optical devices.

Acknowledgments

The authors gratefully acknowledge for financial support: IdEx Bordeaux (Cluster of Excellence LAPHIA and Visiting Scholar support) and the CNRS project EMERGENCE@INC2019. Facilities from the platform SIV.

This project has received funding from the European Union's Horizon 2020 research and innovation programme under the Marie Skłodowska-Curie grant agreement No 823941 (FUNGLASS). This article reflects only the author's view and that the Agency is not responsible for any use that may be made of the information it contains.

References

[1] De Pietro, G. M.; Pereira, C.; Gonçalves R. R.; Ribeiro, S. J. L.; Freschi, C. D.; Cassanjes F. C.; Poirier, G. Thermal, Structural and Crystallization Properties of New Tantalum Alkali-Germanate Glasses. *J.Am.Cer.Soc*. **2015**, 1-8.

[2] Marcondes, L. M.; Maestri, S. A.; De Sousa, B. P.; Gonçalves, R. R.; Cassanjes, F. C.; Poirier, G. High Niobium Oxide Content in Germanate Glasses: Thermal, Structural and Optical Properties. *J.Am.Cer.Soc*. **2018**, *101*, 220-230.

[3] Marcondes, L. M.; Da Cunha, C. R.; Maestri, S. A.; De Sousa, B. P.; Gonçalves, R. R.; Cassanjes, F. C.; Poirier, G. Thermal and Spectroscopic Properties Studies of Er^{3+}-doped and Er^{3+}/Yb^{3+}-codoped niobium germanate glasses for optical applications. *J.Lum.* **2019**, *205*, 487-494.

[4] Da Cunha, C. R.; Maestri, S. A.; De Sousa, B. P.; Marcondes, L. M.; Gonçalves, R. R.; Cassanjes, F. C.; Poirier, G. Alkali Metal Tantalum Germanate Glasses and Glass-Ceramics Formation. *J.Non-Cryst.Sol.* **2018**, *499*, 401-407.

[5] Guedes, L. F. N.; Marcondes, L. M.; Evangelista, R. O.; Batista, G.; Mendoza, V. G.; Cassanjes, F. C.; Poirier, G. Effect of Alkaline Modifiers on the Structural, Optical and Crystallization Properties of Niobium Germanate Glasses and Glass-Ceramics. *Opt.Mat.* **2020**, *105*, 109866.

[6] Marcondes, L. M.; Rodrigues, L.; Da Cunha, C. R.; Gonçalves, R. R.; Camargo, A. S. S.; Cassanjes, F. C.; Poirier, G. Rare Earth Ion Doped Niobium Germanate Glasses and Glass-Ceramics for Optical Device Applications. *J.Lum.* **2019**, *213*, 224-234.

[7] Marcondes, L. M.; Evangelista, R. O.; Gonçalves, R. R.; Camargo, A. S. S.; Manzani, D.; Nalin, M.; Cassanjes, F. C.; Poirier, G. Er^{3+}-doped Niobium Alkali Germanate Glasses and glass-Ceramics: NIR and Visible Luminescence Properties. *J.Non-Cryst.Sol.* **2019**, *521*, 119492.

[8] Marcondes, L. M.; Santagneli, S. H.; Manzani, D.; Cassanjes, F. C.; Batista, G.; Mendoza, V. G.; Da Cunha, C. R.; Poirier, G.; Nalin, M. High Tantalum Oxide Content in Eu^{3+}-doped Phosphate Glass and Glass-Ceramics for Photonic Applications. *J.Al.Comp.* **2020**, 842, 155853.

[9] Marcondes, L. M.; Da Cunha, C. R.; De Pietro, G. M.; Manzani, D.; Gonçalves, R. R.; Batista, G.; Cassanjes, F. C.; Poirier, G. Multicolor tunable and NIR broadband emission from rare-earth-codoped tantalum germanate glasses and nanostructured glass-ceramics. *J.Lum.* **2021**, *239*, 118357.

[10] R. Alvarado, L. Karam, R. Dahmani, A. Lepicard, F. Calzavara, A. Piarristeguy, A. Pradel, T. Cardinal, F. Adamietz, E. Fargin, M. Chazot, K. Richardson, L. Vellutini, and M. Dussauze, "Patterning of the Surface Electrical Potential on Chalcogenide Glasses by a Thermoelectrical Imprinting Process," *J.Phys.Chem.C* **124**, 23150–23157 (2020).

[11] L. Karam, F. Adamietz, D. Michau, C. Gonçalves, M. Kang, R. Sharma, G. S. Murugan, T. Cardinal, E. Fargin, V. Rodriguez, K. A. Richardson, and M. Dussauze, "Electrically Micro-Polarized Amorphous Sodo-Niobate Film Competing with Crystalline Lithium Niobate Second-Order Optical Response," Advanced Optical Materials **8**, 2000202 (2020).

[12] L. Karam, F. Adamietz, D. Michau, G. S. Murugan, T. Cardinal, E. Fargin, V. Rodriguez, K. A. Richardson, and M. Dussauze, "Second-Order Optical Response in Electrically Polarized Sodo-Niobate Amorphous Thin Films: Particularity of Multilayer Systems," Adv Photo Res 2000171 (2021).

[13] A. Lepicard, F. Bondu, M. Kang, L. Sisken, A. Yadav, F. Adamietz, V. Rodriguez, K. Richardson, and M. Dussauze, "Long-lived monolithic micro-optics for multispectral GRIN applications," Sci Rep **8**, 7388 (2018).

[14] Myers, R. A.; Mukherjee, N.; Brueck, S. R. J. Large 2nd-order Nonlinearity in Poled Fused-Silica. *Opt.Lett.* **1991**, *16*, 1732.

[15] Kazansky, P. G.; Russel, P. S. J. Thermally Poled Glass-Frozen-in Electric Field or Oriented Dipoles. *Opt.Commun.* **1994**, *110*, 611.

[16] Mukherjee, N.; Myers, R. A.; Brueck, S. R. J.. Dynamics of Second-Harmonic Generation in Fused Silica. *J.Opt.Soc.Am.B* **1994**, *11*, 665.

[17] Pruneri, V.; Samoggia, F.; Bonfrate, G.; Kazansky, P. G.; Yang, G. M. Thermal Poling of Silica in Air and under Vacuum: The Influence of Charge Transport on Second Harmonic Generation. *Appl.Phys.Lett.* **1999**, *74-17*, 2423-2425.

[18] Lepicard, A.; Cardinal, T.; Fargin, E.; Adamietz, F.; Rodriguez, V.; Richardson, K.; Dussauze, M. Surface Reactivity Control of a Borosilicate Glass using Thermal Poling. *J.Phys.Chem.C* **2015**, *119-40*, 22999-23007.

[19] Quiquempois, Y.; Godbout, N.; Lacroix, S. Model of Charge Migration during Thermal Poling in Silica Glasses: Evidence of a Voltage Threshold for the Onset of a Second-Order Nonlinearity. *Phys.Rev.A* **2002**, *65-4*, 043816-B.

[20] Dussauze, M.; Rodriguez, V.; Lipovskii, A.; Petrov, M.; Smith, C.; Richardson, K.; Fargin, E.; Cardinal, T.; Kamitsos, E. I. How Does Thermal Poling affect the Structure of Soda-Lime Glass? *J.Phys.Chem.C* **2010**, *114-29*, 12754-12759.

[21] Dussauze, M.; Cremoux, T.; Adamietz, F.; Rodriguez, V.; Fargin, E.; Yang, G.; Cardinal, T. Thermal Poling of Optical Glasses: Mechanisms and Second-Order Optical Properties. *Int.Journal.Appl.Glass.Sci.* **2012**, *3*, 309-320.

[22] Moncke, D.; Dussauze, M.; Kamitsos, E. I.; Varsamis, C. P. E.; Ehrt, D. Thermal Poling induced Structural Changes in Sodium Borosilicate Glasses. *Phys.Chem.Glas.* **2009**, *50-3*, 229-235.

[23] Redkov, A. V.; Melehin, V. G.; Lipovskii, A. How does Thermal Poling produce Interstitial Oxygen Silicate Glasses? *J.Phys.Chem.C* **2015**, *119-30*, 17298-17307.

[24] Cremoux, T.; Dussauze, M.; Fargin, E.; Cardinal, T.; Talaga, D.; Adamietz, F.; Rodriguez, V. Trapped Molecular Oxygen and Ionic Species in Poled Borosilicate Glasses: Toward a Rationalized Description of Thermal Poling in Glasses. *J.Phys.Chem.C* **2014**, *118-7*, 3716-3723.

[25] Luo, J. W.; He, H. T.; Podraza, N. J.; Qian, L. M.; Pantano, C. G.; Kim, S. H. Thermal Poling of Soda-Lime Silica Glass with Nonblocking Electrodes Part 1: Effects of Sodium Ion Migration and Water Ingres son Glass Surface Structure. *J.Am.Cer.Soc.* **2016**, *99-4*, 1221-1230.

[26] Smith, N. J.; Pantano, C. G. Structural and Compositional Modification of a Barium Boroaluminosilicate Glass Surface by Thermal Poling. *Appl.Phys.A-Mat.Sci.Proc.* **2014**, *116-2*, 529-543.

[27] McLaren, C.; Balabajew, M.; Gellert, M. Depletion Layer Formation in Alkali Silicate Glasses by Electro-Thermal Poling. *J.electrochem.Soc.* **2016**, *163-9*, H809-H817.

[28] Li, G. Y.; Winick, K. A.; Said, A. A. Waveguide Electro-Optic Modulator in Fused Silica Fabricated by Femtosecond Laser Direct Writing and Thermal Poling. *Opt.Lett.* **2006**, *31-6*, 739-741.

[29] Li, G. Y.; Winick, K. A.; Said, A. A.; Dugan, M.; Bado, P. Quasi-Phase Matched Second-Harmonic Generation through thermal Poling in Femtosecond Laser-Written Glass Waveguides. *Opt.Exp.* **2009**, *17-11*, 9442-9453.

[30] Lipovskii, A. A.; Kuittinen, M.; Karvinen, P.; Leinonen, K.; Mehelin, V. G.; Zhurikhina, V. V.; Zvirko, Y. P. Electric Field imprinting of Sub-micron Patterns in Glass-Metal Nanocomposites. *Nanotech.* ***2008***, 19.

[31] Chervinskii, S., Sevriuk, V., Reduto, I.; Lipovskii, A. Formation of 2d-Patterning of Silver Nanoisland Film using Thermal Poling and Out-Diffusion from Glass. *J.Appl.Phys.* **2013**, 114.

[32] Lipovskii, A. A.; Rusan, V. V.; Tagantsev, D. K. Imprinting Phase/Amplitude Patterns in Glasses with Thermal Poling. *Sol.State.Ionics* **2010**, *181*, 849-855.

[33] Yang, G.; Dussauze, M.; Rodriguez, V.; Adamietz, F.; Marquestaut, N.; Deepak, K. L. N.; Grojo, D.; Uteza, O.; Delaporte, P.; Cardinal T.; Fargin, E. Large Scale Micro-structured Optical Second Harmonic Generation Response Imprinted on Glass Surface by Thermal Poling. *J.Appl.Phys.* **2015**, *118-4*, 043105.

[34] Brunkov, P. N.; Melekhin, V. G.; Goncharov, V. V.; Lipovskii, A. A.; Petrov, M. I. Submicron-Resolved Relief Formation in Poled Glasses and Glass-Metal Nanocomposites. *Tech.Phys.Lett* **2008**, *34-12*, 1030-1033.

[35] Redkov, A. V.; Melehin, V. G.; Statcenko, V. V.; Lipovskii, A. A. Nanoprofiling of Alkali-Silicate Glasses by Thermal Poling. *J.Non.Cryst.Sol.* **2015**, *409*, 166-169.

[36] Dussauze, M.; Rodriguez, V.; Adamietz, F.; Yang, G.; Bondu, F.; Lepicard, A.; Chafer, M.; Cardinal, T.; Fargin, E. Accurate Second Harmonic Generation Microimprinting in Glassy Oxide Materials. *Adv.Opt.Mat.* **2016**, *4*, 929-935.

[37] L. Karam, F. Adamietz, D. Michau, C. Gonçalves, M. Kang, R. Sharma, G. S. Murugan, T. Cardinal, E. Fargin, V. Rodriguez, K. A. Richardson, and M. Dussauze, "Electrically Micro-Polarized Amorphous Sodo-Niobate Film Competing with Crystalline Lithium Niobate Second-Order Optical Response," Advanced Optical Materials **8**, 2000202 (2020).

[38] Poirier, G.; Dussauze, M.; Rodriguez, V.; Adamietz, F.; Karam, L.; Cardinal, T.; Fargin, E. Second Harmonic Generation in Sodium Tantalum Germanate Glasses by Thermal Poling. *J.Phys.Chem.C* **2019**, *123-43*, 26528-26535.

[39] Q. Li, "Optimization of point spread function of a high numerical aperture objective lens : application to high resolution optical imaging and fabrication," Degree Thesis, ENS Cachan (2014).

[40] Henderson, G. S.; Fleet, M. E. The Structure of Glasses along the Na2O-GeO2 Join. *J.Non.Cryst.Sol.* **1991**, *134*, 259-269.

[41] Monteiro, G.; Santos, L. F.; Pereira, J. C. G.; Almeida, R. M. Optical and Spectroscopic Properties of Germanotellurite Glasses. *J.Non.Cryst.Sol.* **2011**, *357*, 2695-2701.

[42] Peng, J.; Cao, J.; Tan, L.; Peng, M. Glass-forming Region and Enhanced Bi NIR Emission in Sodium Tantalum Silicate Laser Glass. *J.Am.Cer.Soc.* **2019**, *102*, 2522-2530.

[43] Wetherall, K. M.; Doughty, P.; Mountjoy, G.; Bettinelli, M., Speghini, A.; Casula, M. F.; Cesare-Marincola, F.; Locci, E.; Newport, R. J. The Atomic Structure of Niobium and Tantalum containing Borophosphate Glasses. *J.Phys.Cond.Mat.* **2009**, *21*, 375106.

[44] Guimbretière, G.; Dussauze, M.; Rodriguez, V.; Kamitsos, E. Correlation between Second-Order Optical Response and Structure in Thermally Poled Sodium Niobium-Germanate Glass. *Appl.Phys.Lett.* 2010, *97.*

[45] Karam, L.; Adamietz, F.; Rodriguez, V.; Bondu, F.; Lepicard, A.; Cardinal, T.; Fargin, E.; Richardson, K. and Dussauze, M. The effect of the sodium content on the structure and the optical properties of thermally poled sodium and niobium borophosphate glasses. *J.Appl.Phys.* 2020, 128, 043106.

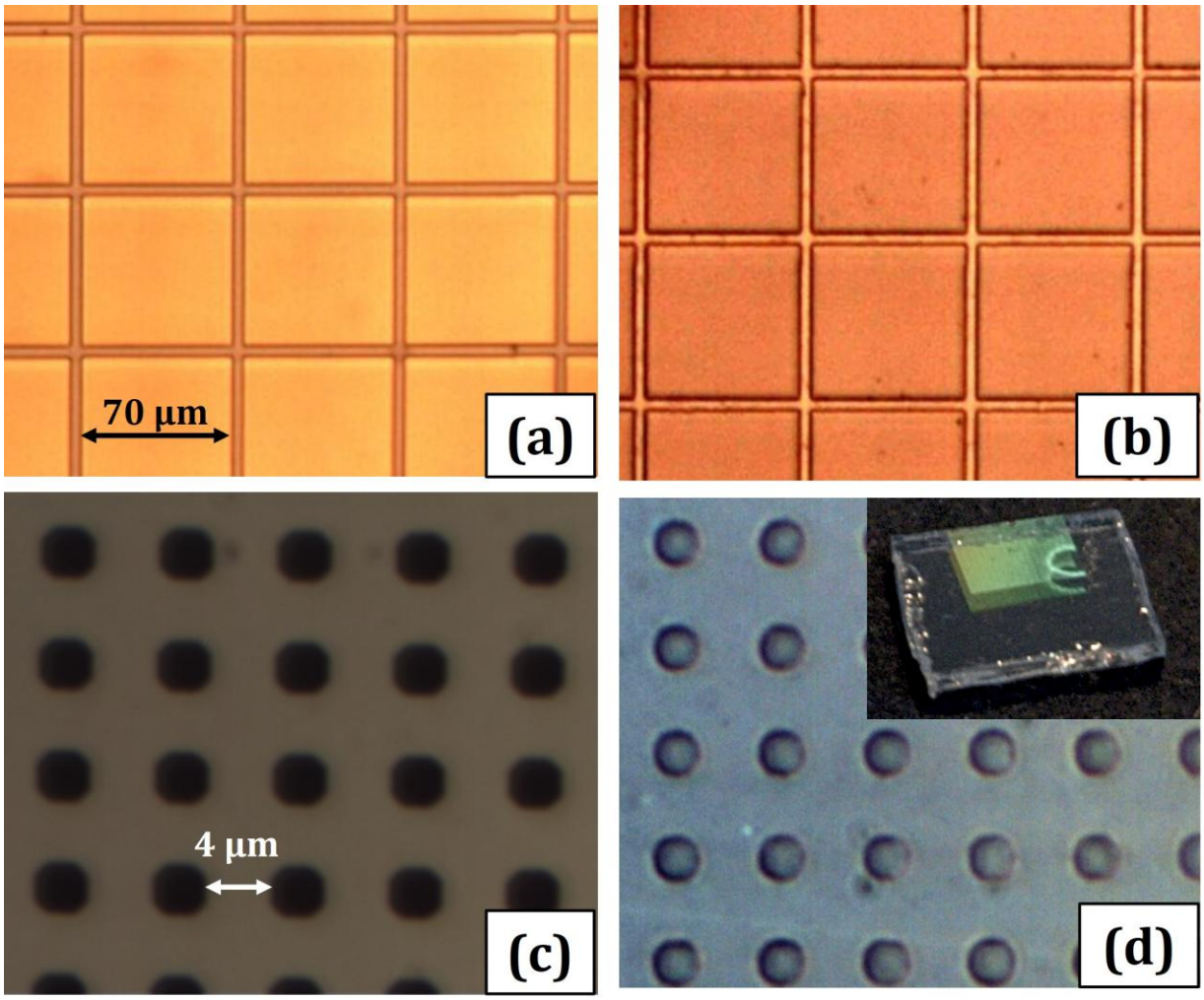

Figure 1. Optical micrographs of the surface of (a) electrode E-70/4, (b) glass sample G-70/4, (c) electrode E-4/4 and (d) glass sample G-4/4.

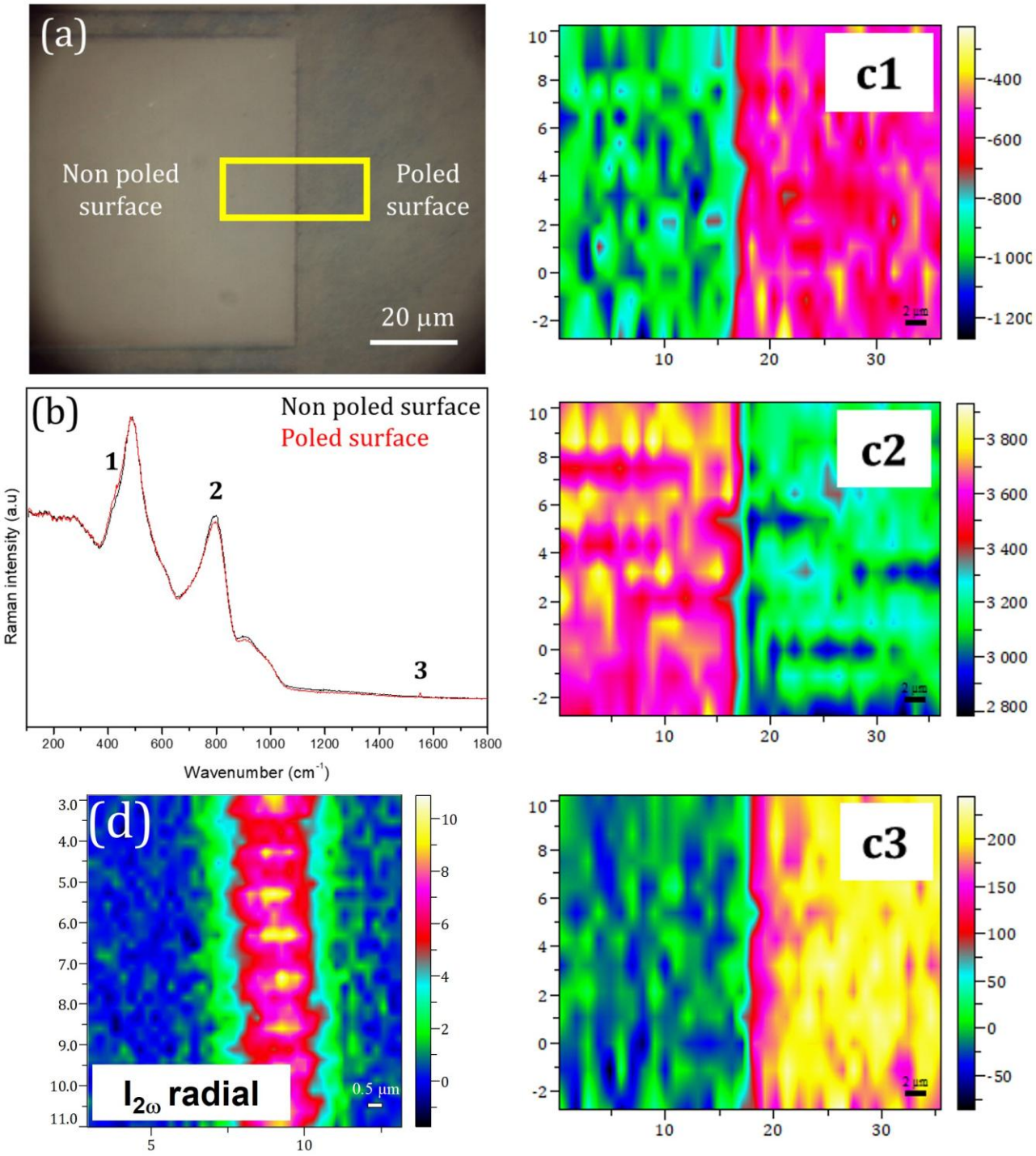

Figure 2. (a) Optical micrograph of the sample 70/4 and studied area, (b) Raman spectra in the unpoled and poled surfaces, (c1) µ-Raman maps for Raman mode 1, (c2) mode 2 and (c3) mode 3 highlighted in b and (d) µ-SHG map of the corresponding studied area under radial polarization.

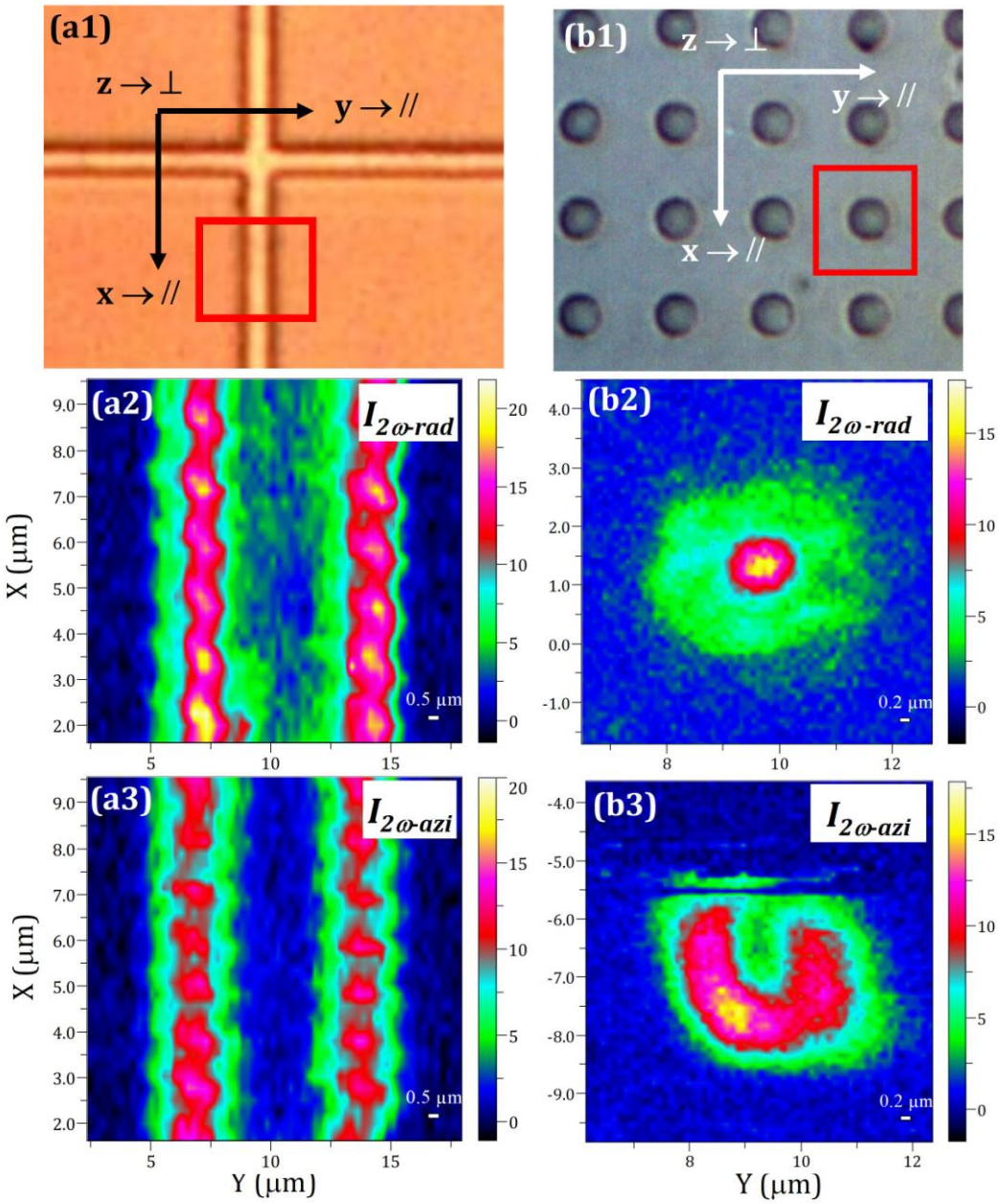

Figure 3. Optical micrographs of poled samples (a1) G-70/4, (b1) G-4/4 with studied areas in red, (a2) and (b2) respective µ-SHG maps for radial polarization, (a3) and (b3) respective µ-SHG maps for azimuthal polarization, (a4) and (b4) respective SHG intensity profiles along the y direction for radial and azimuthal polarizations,

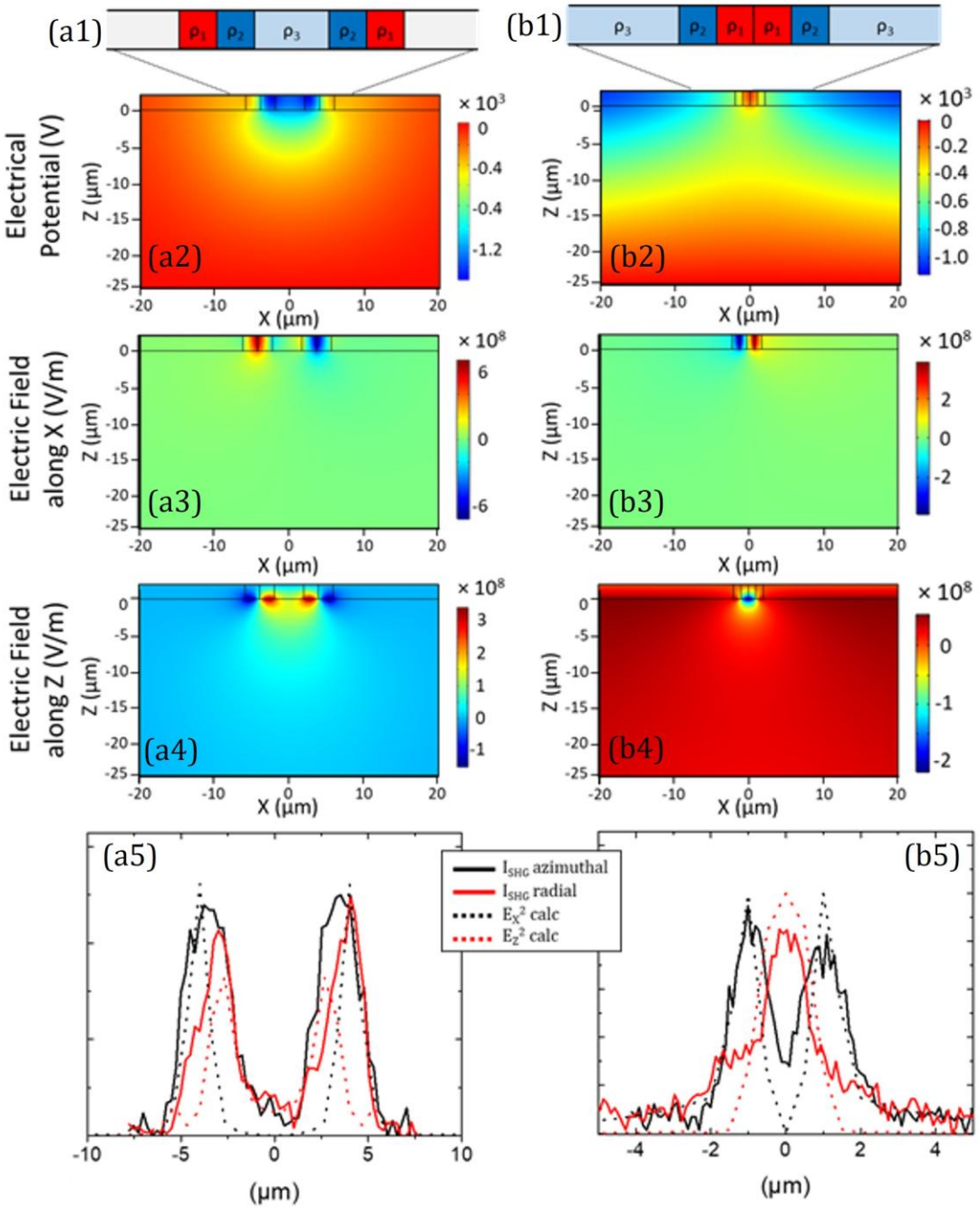

Figure 4. Scheme of the electrostatic model of charge distribution and resulting field enhancement at the boundaries between poled and unpoled areas for (a1) sample G-70/4 and (b1) sample G-4/4. Areas labeled ρ_1, ρ_2 and ρ_3 denote different charge concentrations at the boundaries between poled and unpoled surfaces. Corresponding electric potentials for (a2) G-70/4 and (b2) G-4/4, corresponding

electric fields along x and z for (a3), (a4) sample G-70/4 and (b3), (b4) sample G-4/4. SHG intensity comparison between experimental data and theoretical values calculated using the electrostatic model for (a5) sample sample G-70/4 and (b5) sample G-4/4.

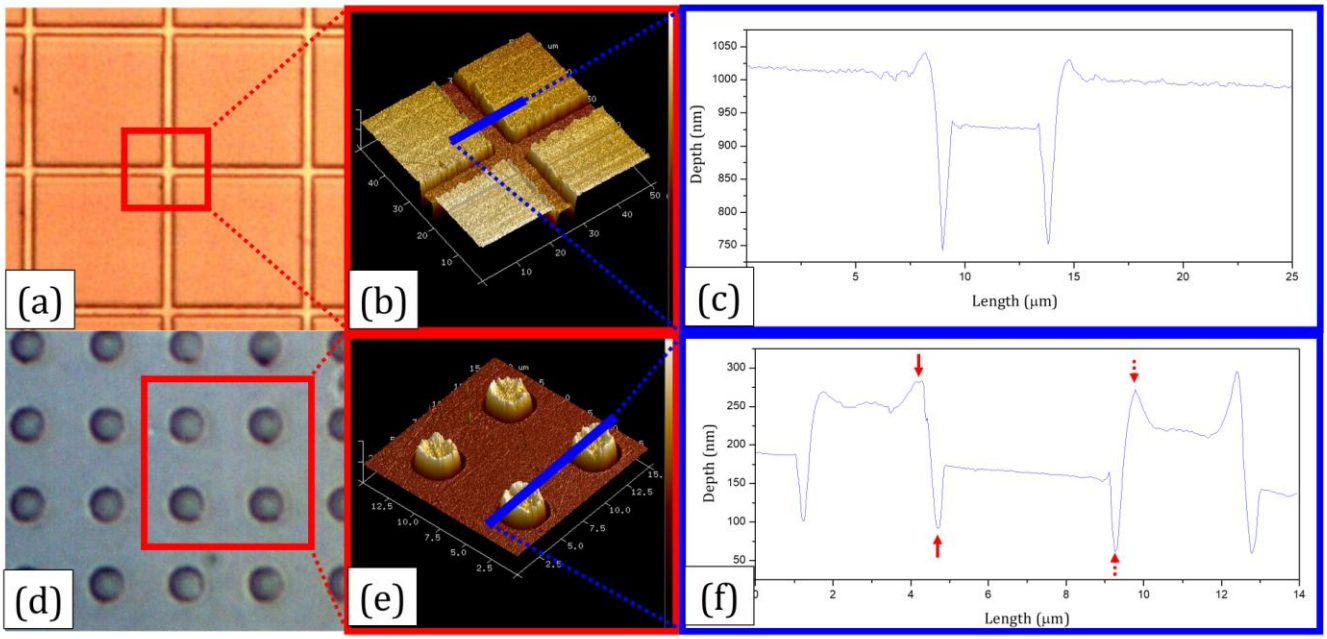

Figure 5. (a) and (d) Optical micrographs of the studied area in samples G-70/4 and G-4/4, (b) and (e) 3D AFM images of the respective studied areas, (c) and (f) AFM profiles along the blue lines.

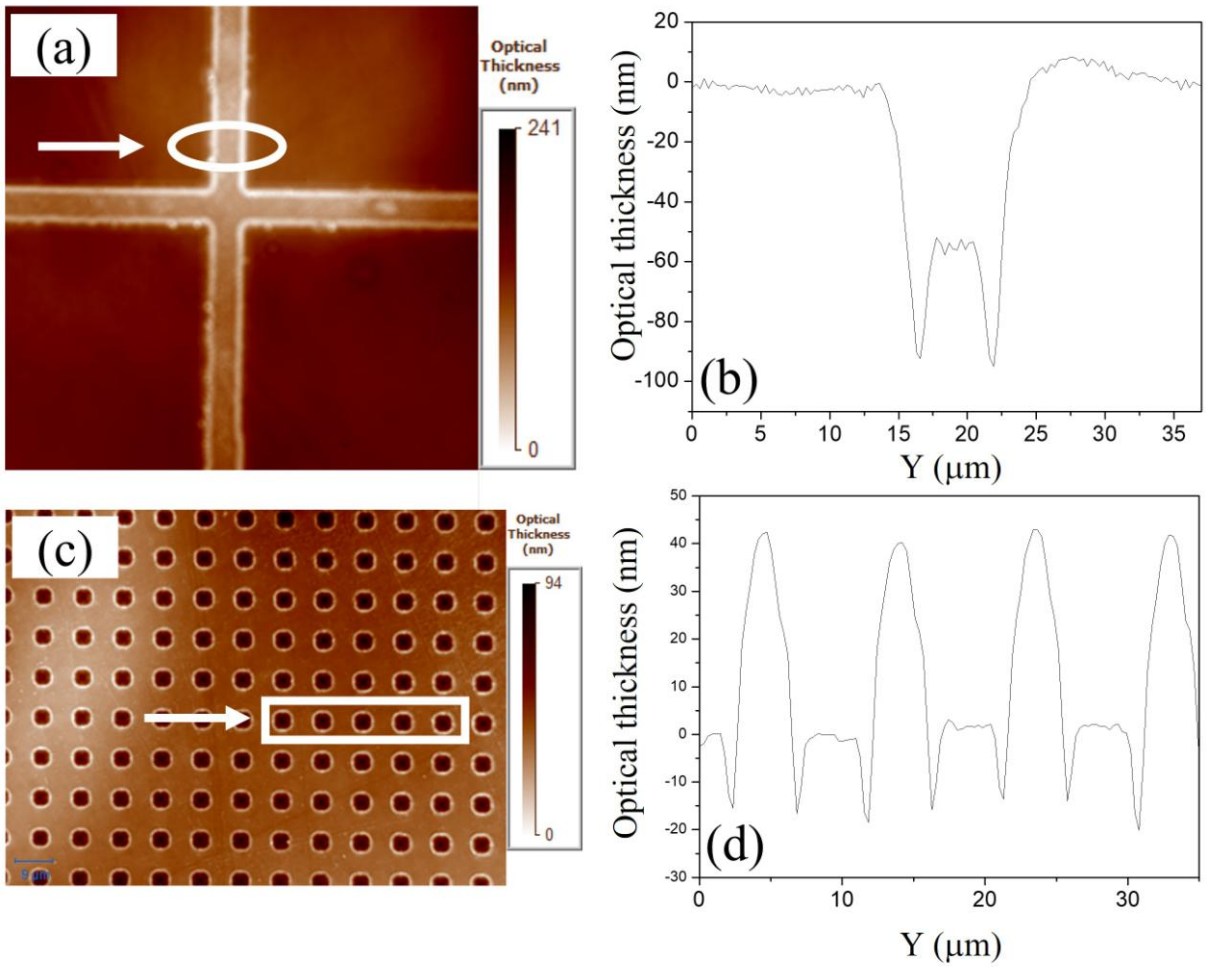

Figure 6. (a) and (c) Phase contrast images in samples G-70/4 and G-4/4, (b) and (d) respective optical thickness profiles along the poled cross-section shown by the white arrows.

Supplementary Material S1: Intensity distribution profiles of the incident azimuthally (left) or radially (right) polarized beam in the focal region. The profiles were calculated for a 1064 nm incident beam corresponding to the two different objectives employed in this work with numerical apertures of respectively 0.9 in air (top) and of 1.3 in oil (bottom)

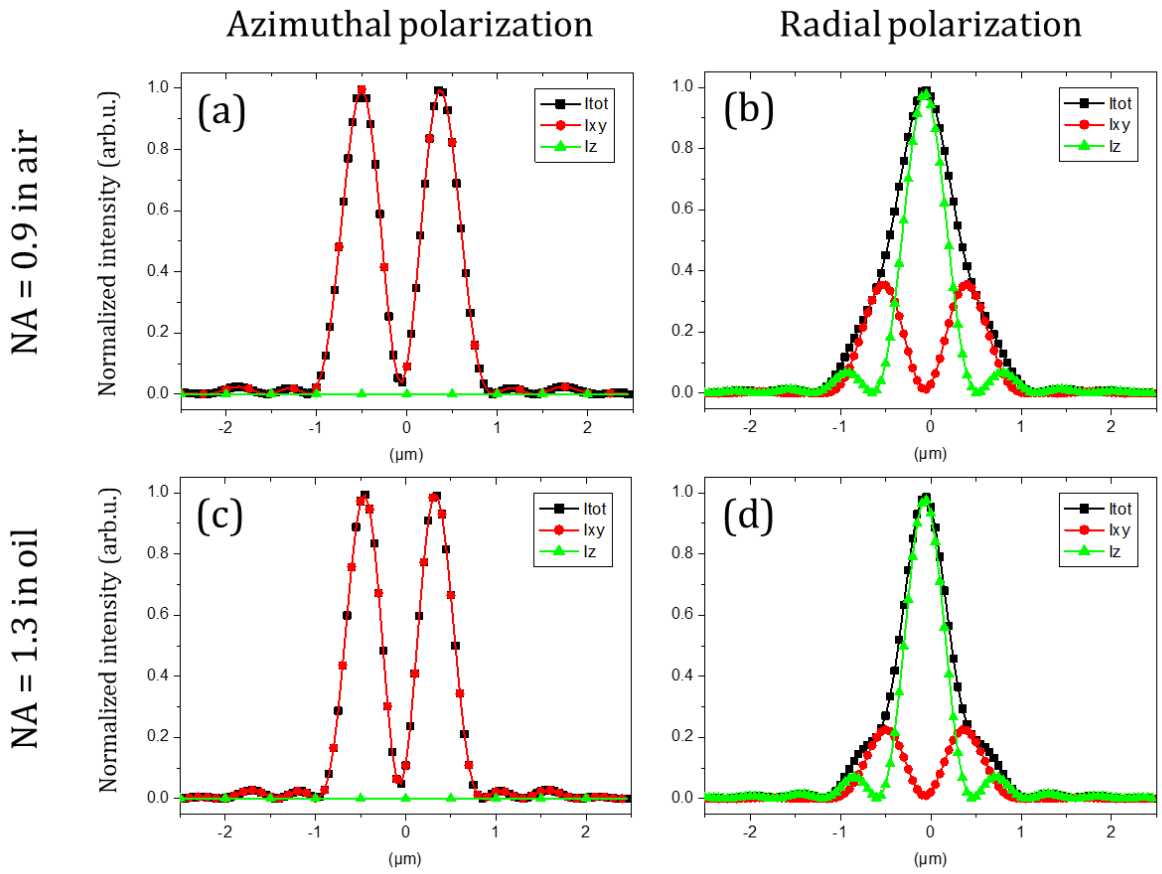

Supplementary Material S2: Schematic of Δn estimation taking into account topology corrections.

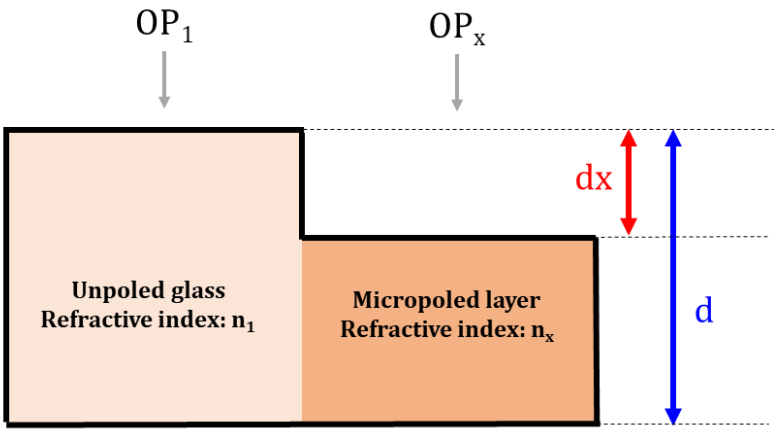

d_x : topological depth (measured by AFM)

d >>> d_x and can be considered to be 2.5 µm (poled layer measured by SHG microscopy) [38]

n_1 = 1.83 (measured by the Brewster angle) [38]

$OP_1 = n_1.d$

$OP_x = n_x.(d-d_x) + n_{air}.d_x = n_1.(d-d_x) + d_x$

$OPD = OP_x - OP_1$

Then:

$$n_x = \frac{OPD - dx + n_1.d}{d - dx}$$

And:

$\Delta n = n_x - n_1$

Sample	**G-70/4**	**G-4/4**
n_1	1.83	1.83
d	2.5 µm	2.5 µm
d_x (Figure 5)	100 nm	75 nm
OPD (Figure 6)	60 nm	45 nm
n_x	1.839	1.837
Δn	0.009	0.007